Materials Today Sustainability 34 (2026) 101352

Contents lists available at ScienceDirect

Materials Today Sustainability

journal homepage: www.journals.elsevier.com/materials-today-sustainability

Upcycling post-consumer PET bottles into low-density films and 3D-printed materials

M. Merillas [a,b], J. Lledó [a,b], M. Santiago-Calvo [c], L. Matesanz-Niño [c], J. Martín-de León [a,b,*], J.C. Merino [c], M.A. Rodríguez-Pérez [a,b]

[a] Cellular Materials Laboratory (CellMat), Condensed Matter Physics Department, University of Valladolid, Valladolid, 47011, Spain
[b] BioEcoUVA Research Institute on Bioeconomy, University of Valladolid, Spain
[c] Foundation for Transport and Energy Research and Development (CIDAUT), Technological park of Boecillo, Boecillo, 47151, Spain

ARTICLE INFO

Keywords:
Recycled polyethylene terephthalate
3D printing
Foaming

ABSTRACT

Recycled polyethylene terephthalate (rPET) from mixed-color bottle waste is typically downcycled due to its variable composition and reduced melt strength, limiting their contribution to circular economy strategies and high-value applications. In this work it is proved that gas dissolution foaming enables the upcycling of two industrial rPET, light-blue PET (PET_B) and color recycled PET (PET_C) into low-density microcellular films and 3D printed-parts. A comprehensive materials characterization allows to establish the optimum processing window for these materials. This way optimized microcellular structures were produced at mild saturation conditions (15 MPa, 50 °C). PET_B shows cell sizes close to 2 μm together with relative densities of 0.2 to 0.28, outperforming virgin PET. PET_C, despite containing several non-miscible contaminants, also leads to stable cellular materials with cell sizes from 5 to 18 μm. Finally, we demonstrate for the first time that rPET 3D-printed components can be foamed while preserving their overall geometry, undergoing a controlled volumetric expansion and achieving a 40% density reduction with homogeneous microcellular structure. Overall, this study highlights the potential of gas dissolution foaming as a robust upcycling route for heterogeneous PET waste streams, enabling lightweight materials and supporting circular manufacturing strategies.

1. Introduction

The increasing consumption of plastic materials has led to significant environmental concerns due to its slow degradation and excessive accumulation in landfills and marine ecosystems. Particularly polyethylene terephthalate (PET) accounted for approximately 6% of the global demand for plastics, making it one most in-demand plastic material in 2022 [1].

Recycled PET (rPET) has emerged as a sustainable alternative, allowing for the reduction of virgin plastic production while maintaining desirable material properties for various applications, such as 3D printing, packaging, textiles, and automotive components [2], [3]. The implementation of rPET aligns with the principles of the circular economy, a model aimed at minimizing waste and resource consumption by promoting recycling, reusability, and closed-loop material flows [4]. Enhancing rPET use not only mitigates environmental pollution but also contributes to lowering carbon emissions and energy consumption associated with virgin PET manufacturing [5].

However, reusing PET is not an easy task, particularly when talking about blue, or mixed-color rPET post-consumer, due to its variability and complexity in composition as it contains dyes, labels or other plastics, inconsistent material properties and reduced market value. Unlike clear PET, whose repurpose into high-quality applications is usually more straightforward, usually color and mixed-color rPET require additional sorting and processing to maintain acceptable aesthetic and mechanical properties [6]. On the other hand, advanced chemical recycling methods, such as depolymerization, are being explored to improve rPET quality but remaining cost and being energy-intensive [7]. As a result, mixed-color rPET is often downcycled into low-value applications, limiting its potential within a circular economy [8]. Lightweight cellular structures represent an attractive route to add value to these under-utilized rPET streams, provided that stable and controllable foaming processes can be achieved.

Extrusion foaming of rPET has been widely studied as a sustainable approach to reuse this material by producing lightweight polymeric foams. However, one of the main challenges in rPET extrusion foaming

* Corresponding author. Cellular Materials Laboratory (CellMat), Condensed Matter Physics Department, University of Valladolid, Valladolid, 47011, Spain.
E-mail address: judit.martin.leon@uva.es (J. Martín-de León).

https://doi.org/10.1016/j.mtsust.2026.101352
Received 13 January 2026; Received in revised form 23 February 2026; Accepted 23 March 2026
Available online 25 March 2026

is the formation of large cell sizes, which can affect the material's mechanical properties and thermal insulation capabilities. The use of supercritical CO_2-assisted extrusion has been explored to improve cell morphology, for example, Bocz et al. use chain extenders and nucleating agents such as talc helping to refine cell structures leading to 200 μm cells [9]. Additionally, long-chain branched (LCB) PET has been found to significantly enhance foamability by increasing melt strength and reducing cell size up to 18 μm during foaming [10]. Despite these advancements, color or mixed-color rPET has not been widely used in extrusion foaming, likely due to inconsistencies in material properties and poor aesthetic appeal, which can limit its applicability in high-value markets [11]. Despite these advances, the foaming of mixed-color rPET remains scarcely explored, and alternative foaming routes capable of handling material heterogeneity are still missing.

Additionally, to extrusion foaming, rPET has been also used in injection and batch foaming, but achieving small cell sizes remains a challenge, especially if a second phase is not added. Factors such as matrix viscosity, cooling conditions, and gas concentration influence cell nucleation and growth. Studies indicate that even with process optimizations, cell sizes do not fall below 25 μm due to cell coalescence and structural limitations [9], [12], [13]. These constraints highlight the need for further advancements in rPET foaming technologies to achieve finer cellular structures.

Solid-state gas dissolution foaming has proven to be a powerful technique to produce micro- and nanocellular structures in polymers with limited melt strength. However, its application to recycled PET—particularly mixed-color post-consumer streams and 3D-printed parts—has not been reported to date.

In this work, we proved for the first time that upcycling color and mixed-color rPET films is feasible using the gas dissolution foaming technique. Optimizing the production parameters allows the production of low-density recycled materials, also with cell sizes significantly smaller than those previously reported in the literature. Furthermore, this work proves that this technique enables the fabrication of low-density foamed 3D-printed rPET parts while preserving their original shape. This advancement highlights the potential of upcycling PET from bottles to contribute to a more sustainable and environmentally friendly future.

2. Experimental

2.1. Materials

Under-value recycled PET from a mix of colored bottles, concretely light blue and color, was acquired from ClearPET (Valencia, Spain) in the form of flakes. Light blue rPET (PET_B) belongs to a stream of recycled PET that mostly contains blue and transparent flakes from bottle waste. The characteristics of PET_B are detailed as follows: intrinsic viscosity of 0.70-0.80 dl/g, bulk density of 300-350 kg/m^3, size distribution of flakes between 1 mm and 10 mm (99.9% of flakes), and several impurities (metal <10 ppm, labels <150 ppm, PVC <50 ppm, polyolefins <50 ppm, flake with glue <1500 ppm, glue <200 ppm and other colors <1500 ppm). Color recycled PET (PET_C) comes from PET bottle colored streams. The color flakes have a particle size below 1 mm, a bulk density of 300-350 kg/m^3, and various impurities (metal <250 ppm, labels (on PVC) < 1500 ppm, PVC <500 ppm, polyolefins <250 ppm, pigment <1000 ppm and other colors between 5 and 10%). Virgin PET (PET_V) purchased from NOVAPET (reference SPRIT L-21 BB1000) with low viscosity, 0.63 dl/g, was selected as a rheological reference material. This grade was intentionally chosen to exhibit melt viscosity and flow behavior comparable to the degraded recycled PET streams under study. Using a typical bottle-grade PET (0.80 dl/g) would result in significantly higher melt strength, which could bias the interpretation of foaming behavior when comparing with degraded rPET materials. Medical-grade CO_2 (99.9% purity) was used as a blowing agent for the gas dissolution foaming experiments.

2.2. Sample preparation

2.2.1. Extrusion

The recycled materials were dried at 100 °C overnight in a dryer DT 202M (Moretto, Massanzago, Italy) and after that recycled PET flakes were processed using a co-rotating twin-screw extruder, model Leistritz 27 GL (L/D = 36), at a screw temperature profile of 265 °C, a die temperature of 255 °C and 50 rpm. Granulates of blue and color recycled PET (PET_B and PET_C) were obtained to feed the calendaring process. To evaluate the foaming capabilities, films of the two rPET types were prepared using a single-screw extruder, model COLLIN E30P with a calendaring system. The process parameters to obtain films were 150 rpm and temperature profile from 220 °C to 270 °C. Subsequently, the calendar rolls were cooled with water at 8 °C to cool the films and allow subsequent handling. The resulting films presented a thickness of 0.40 mm.

2.2.2. 3D printer

3D printed parts in the shape of bottle caps were designed using PET_B (Fig. 1). The cap-like geometry was selected as a representative three-dimensional model inspired by packaging applications, rather than as a functional closure system. Firstly, 3D printing filaments were obtained from granulates of recycled PET (PET_B). The rPET granulates were subjected to a drying process (24 h at 80 °C) prior to filament preparation. The filament production was carried out in a device consisting of a single-screw extruder (EXE6 FILABOT filament maker) in which the material was processed at 260 °C and 50 rpm, followed by a blower to solidify it and a winding system with a thickness gauge. The filaments obtained have a diameter of around 1.70 ± 0.08 mm. Once the filaments were obtained, the recycled material filaments were then incorporated into a home-made 3D printer machine using fused deposition modeling (FDM) 3D printing. The following print conditions were used: extrusion temperature (260 °C), bed temperature (60 °C), camera temperature (40 °C), printing velocity (30 mm/s), and infill density (100%).

2.2.3. Gas dissolution foaming

The gas dissolution foaming process was used to obtain PET and rPET cellular films and foamed 3D printed parts. The foaming process was carried out in a pressure vessel (model PARR 4681) provided by PARR Instrument Company (Moline, IL, USA). A pressure pump (model SFT-10) provided by Supercritical Fluid Technologies Inc. (Neward, DE, USA) was used to work at different pressures. Thermal baths from Grupo Selecta (Barcelona, Spain) and an air-circulating oven (for the higher foaming temperature) were used to foam the samples after the saturation process.

Gas dissolution foaming consists of four steps. First, the polymer is saturated inside the pressure vessel under a CO_2 atmosphere at certain saturation pressure (p_{sat}) and saturation temperature (T_{sat}). Once the polymer is completely saturated, after the saturation time (t_{sat}), a fast depressurization at a certain depressurization velocity (v_d) is carried out. After a certain desorption time (t_d), samples are foamed by immersion in a silicone hot bath at a selected foaming temperature (T_{foam}) at temperatures below 200 °C, and in a convection oven at temperatures over 200 °C, during the foaming time (t_f). Finally, samples are stabilized at room temperature to avoid degeneration mechanisms.

In the present work, the saturation step was performed at two different p_{sat} (15 and 30 MPa) with a fixed T_{sat} at 50 °C, during a t_{sat} of 69 h in all cases. Depressurization was conducted at a v_d of 40 and 93 MPa/s respectively. After a t_d between 2 and 4 min for all the samples, the foaming step was performed at six different T_{foam} (100, 120, 150, 180, 200 and 220 °C) with a fixed t_f of 1 min.

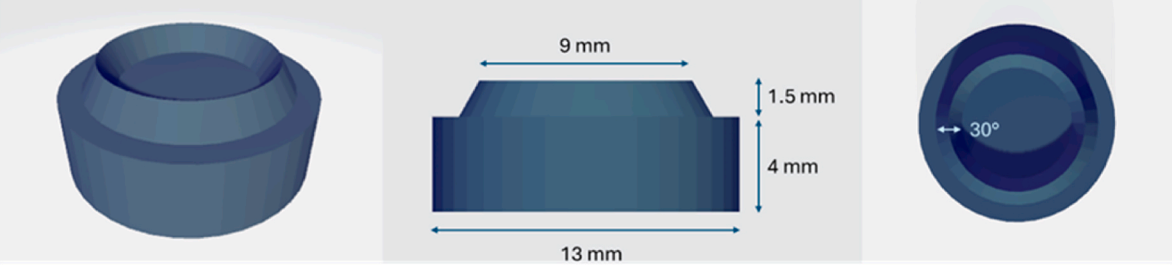

Fig. 1. Design of bottle caps for 3D printer using recycled PET.

2.3. Characterization

2.3.1. MFI

Melt flow index (MFI) from the granulates was measured by using a Melt Flow Tester CEAST MF20 from Instron with a heating chamber set at 260 °C and a load of 1200 g weight [11]. Prior to testing, samples were dried at 80 °C overnight in a dryer DT 202M (Moretto, Massanzago, Italy).

2.3.2. Shear and extensional rheology

HAAKE Rheostress 600 dynamic rheometer was employed to analysis the viscosity in the molten state. The rheological experiments were carried out with a plate-plate geometry of 20 mm and a selecting gap between plates of 1 mm. Firstly, amplitude sweep tests were performed at strains ranging from 0.001% to 100%, with an angular frequency of 5 rad/s and 260 °C, to select a constant strain to measure the three materials in the linear viscoelastic region (LVR). Subsequently, frequency sweep tests were measured at 260 °C, a constant strain of 0.1% and an angular frequency range from 0.5 to 300 rad/s.

Extensional rheology was performed in the solid materials in a stress-controlled rheometer, model AR 2000 EX from TA instruments equipped with an extensional fixture SER 2 from Xpansion Instruments. In this equipment, the samples are secured between two counter-rotating cylinders that apply a uniaxial tensile force to the material at a constant rotation speed. For PET_V and PET_B, experiments were performed at a temperature of 220 °C under varying Hencky strain rates of 0.1, 0.5, 1 and 2.5 s^{-1}. In these experiments, the maximum Hencky strain is 2.8, however, none of the solids withstand such deformations, thus in this work, the maximum deformation is the one sustained by each material. In the case of PET_C the selected temperature was 245 °C (at 220 °C the material breaks in the pre-stretching step) while a unique Hencky strain rate of 1 s^{-1} was used due to lack of reproducibility between samples.

2.3.3. Density

The density of the solid precursors (ρ_s) as well as the final cellular materials (ρ_f) were measured with the water displacement method with a density determination kit for an AT261 Mettler-Toledo balance (Mettler-Toledo, Columbus, OH, USA), based on the Archimedes' principle. The relative density (ρ_r) was calculated as indicated in Equation (1):

$$\rho_r = \frac{\rho_f}{\rho_s} \tag{1}$$

2.3.4. DSC

Differential scanning calorimetry (DSC) tests were performed in a model DSC3+ (Mettler, USA) in order to evaluate the glass transition temperature (T_g), melting temperature (T_m) and crystallinity degree (χ_c) from the solid precursors and the final cellular materials. Tests were conducted in a range of temperatures from −50 to 300 °C, at a rate of 10 °C/min. The crystallinity degree of each sample was calculated using Equation (2):

$$X_c\ (\%) = \frac{\Delta H_m}{\Delta H_{m,0}} \cdot 100 \tag{2}$$

Where ΔH_m is the enthalpy of crystallization per mass, whereas $\Delta H_{m,0}$ is the enthalpy of crystallization of 100% crystalline PET, taken as 140 J/g [14]. The T_g was taken as the mid-point of the drop in the DSC thermogram that characterizes this transition in the first heating step. Furthermore, the T_m was taken as the temperature for the melting peak also in the first heating step [15].

2.3.5. Solubility and diffusivity

The solubility of the samples refers to the percentage of mass gained by the sample due to the gas absorption. The weight of the samples after complete saturation (m_f) can be extrapolated from the desorption curve (mass vs. time$^{1/2}$) [16], which was registered with a Mettler-Toledo balance (Mettler-Toledo, Columbus, OH, USA). The solubility of the samples can be calculated with Equation (3):

$$Solubility\ (\%) = \frac{(m_f - m_0)}{m_0} \cdot 100 \tag{3}$$

Where m_0 is the initial mass of the samples, weighted before the saturation process.

Diffusivity, on the other hand, gives an idea of how fast the gas is diffusing out from the polymer matrix once the saturation is over. It was evaluated from the desorption plot by analyzing the slope of the initial segment of the desorption curve. The diffusivity (D) can be calculated through Equation (4):

$$D = \frac{\pi R^2}{16} \tag{4}$$

Where R is the slope of the initial segment from the desorption curve when representing the mass versus $t^{1/2}$/L, being L the thickness of the sample [17].

2.3.6. Cellular structure

The cellular structure of the samples was visualized through scanning electron microscope (SEM) micrographs, obtained by FlexSEM 100 Hitachi (Tokyo, Japan). In order not to damage the cellular structure, the samples were cooled down in liquid nitrogen prior to fracturing. Then, the fractured surfaces were coated with gold using a sputter coater (model SCD 005, Balzers Union). For analyzing the cellular structure, the SEM images were analyzed by an internally developed software [18] able to measure more than 100 cells per micrograph with appropriate precision. 3D Cell size (ϕ), standard deviation and cell nucleation density (N_0) were obtained from this software according to Kumar method [2]. Samples with cell sizes below 1 μm were analyzed with the software based on ImageJ/FIJI, measuring a satisfactory number of cells, which result obtained from a 2D image was corrected to 3D by multiplying by a factor of 1.273 [3].

3. Results and discussion

3.1. Solid materials

3.1.1. Microstructure

The characterization of the microstructure of the solid precursors was performed as described in section 2.3.6. SEM images from the solid materials are shown in Fig. 2:

Both PET_V and PET_B samples present a homogeneous structure, with no visible impurities. However, in PET_C sample some spheres can be observed when performing SEM micrographs at high magnifications. These spheres appear due to the immiscibility of some of the recycled components and PET [19] [20]. These micrographs prove that PET_C sample is the one with the larger number of impurities. On the other hand, despite being a recycled sample, PET_B presents much fewer visible impurities, and its microstructure seems to be as homogeneous as the PET_V. As it will be discussed later, the presence of these non-miscible components will influence the foamability of these materials.

3.1.2. MFI

The melt flow index for the granules of the three materials under study was characterized to measure the ease of flow of the melt of a thermoplastic polymer. In Table 1, the MFI values for the three samples are collected. It is observed that the PET_V has the highest MFI value, which is expected as virgin material with low intrinsic viscosity to be comparable to the recycled materials that are more degraded. Regarding the recycled materials, the most degraded material (PET_C), which contains more impurities, shows a higher MFI value than the recycled sample PET_B, indicating an increase in melt fluidity. This behavior is in accordance with higher heterogeneity and impurity content observed in PET_C. In post-consumer recycled streams, the presence of degraded fractions and contaminating components can modify the rheological response of the melt, which in some cases favors greater flow during the MFI test, which is subsequently confirmed in the rheological tests of the recycled materials (section 3.1.3).

3.1.3. Shear and extensional rheology

The rheological measurements were carried out for the three materials under study to evaluate the complex viscosity versus angular frequency (Fig. 3). All the materials show similar rheological curves, changing the complex viscosity trends between samples. The rheological curves show a Newtonian plateau at low frequencies followed by a slightly shear thinning region at high frequencies. This rheological behavior corresponds to the typical behavior of polymers with linear molecular structure, which is the case for these materials [21]. The recycled PET_B has higher complex viscosity with angular frequency in comparison to PET_V and PET_C. It is the expected behavior as PET_C is much more degraded than PET_B. In the case of PET_V, it also has a low complex viscosity versus angular frequency as a low viscosity virgin material was selected to be rheologically comparable to the degraded recycled materials, ensuring that differences in foaming behavior are not solely driven by intrinsic viscosity.

Table 1
MFI data of the three granulates materials.

	MFI (g/10 min)
PET_V	46.70 ± 0.68
PET_B	11.52 ± 1.04
PET_C	26.26 ± 2.60

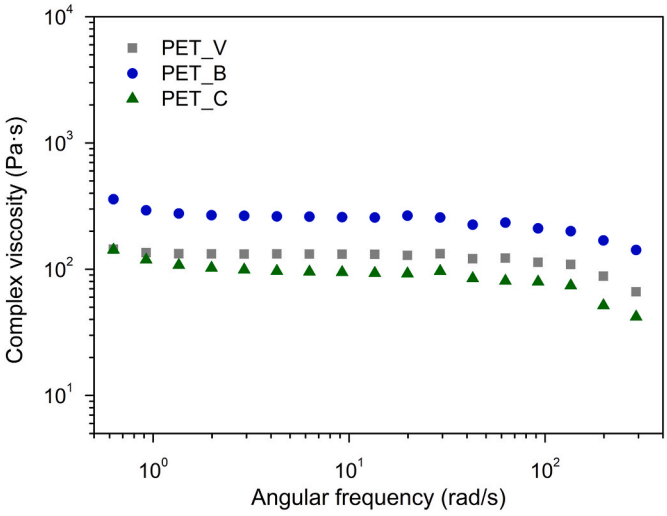

Fig. 3. Complex viscosity versus angular frequency for the three materials (PET_V, PET_B and PET_C).

Fig. 4 shows the results obtained through extensional rheology for the three materials showing the extensional viscosity as a function of time for the different considered Hencky strain rates. In the case of PET_C only a Hencky strain rate was considered showing the results of four curves for different samples of the same material (Fig. 4c).

This behavior could have significant implications if low-density foams are obtained. The lack of strain hardening may promote structural degradation, leading to less homogeneous structures and higher open-cell content. For high densities, this effect will not be as significant. In this work gas dissolution foaming allows the production of cellular materials with no visible cellular degeneration for all the used PETs (section 3.2).

On the other hand, PET_V presents the highest viscosity while PET_C

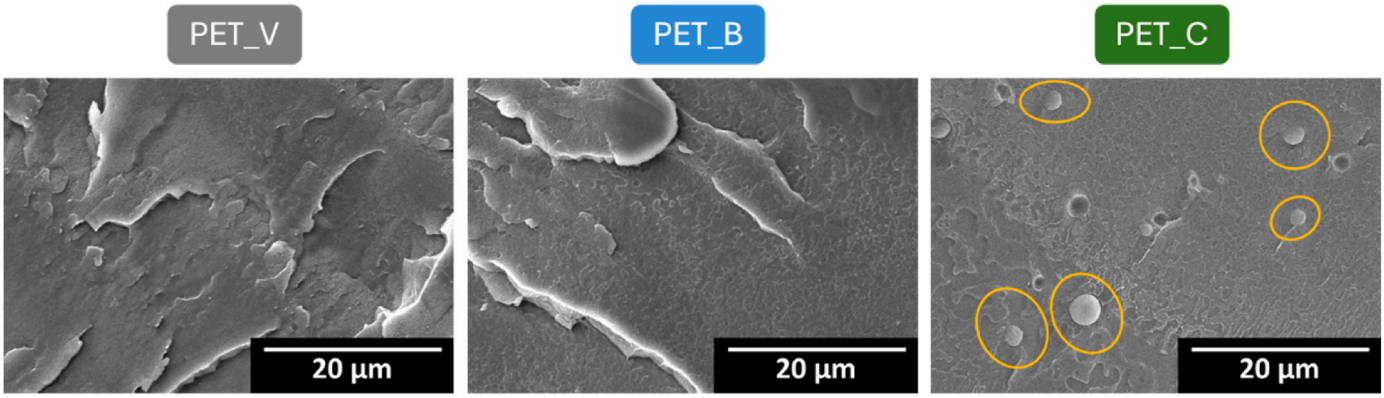

Fig. 2. Magnified SEM images of solid materials.

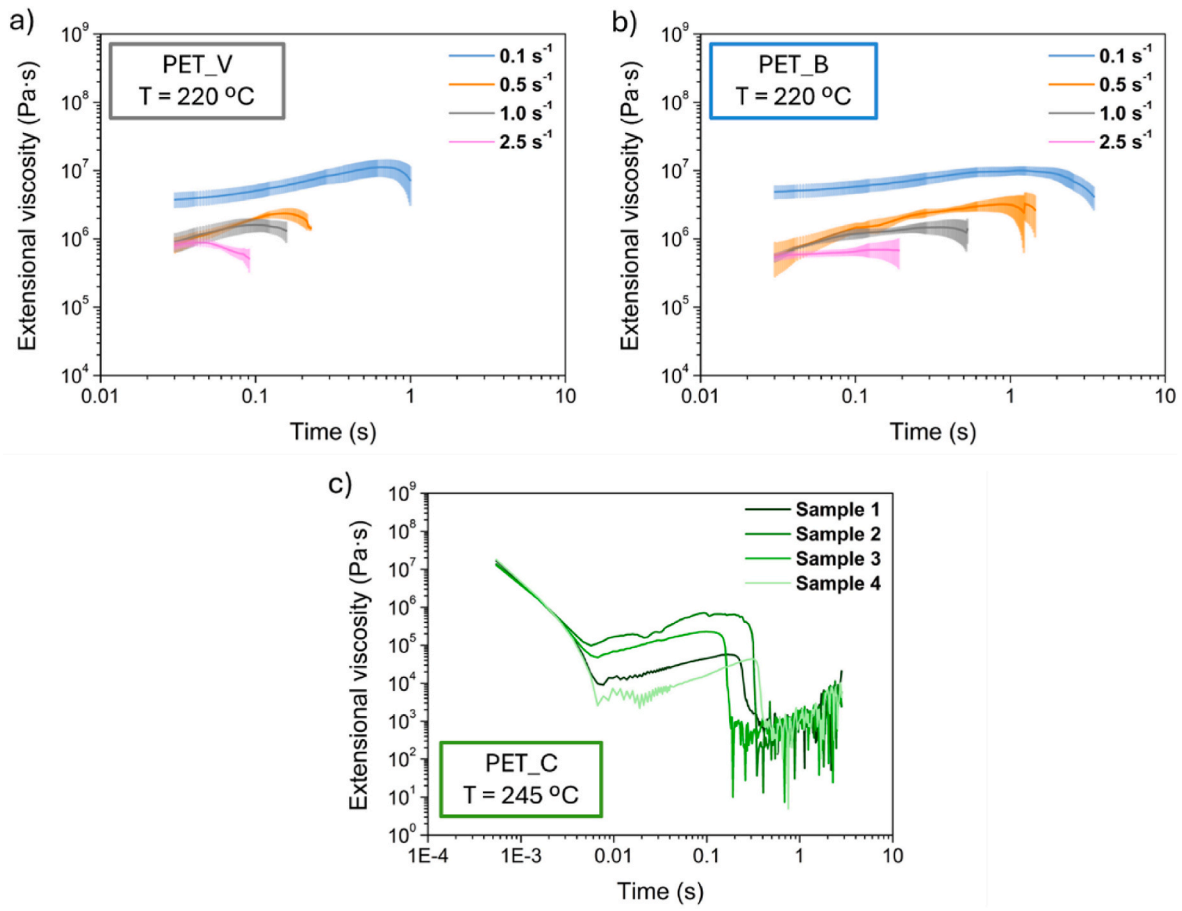

Fig. 4. Extensional viscosity as a function of time for a) PET_V, b) PET_B and c) PET_C. For PET_V and PET_B, the legend indicates each Hencky strain considered. For PET_C, the legend refers to each sample.

present the smallest values, both recycled materials withstand greater deformations than virgin PET, however, none of them reaches the maximum Hencky strain of 2.8 defined for this kind of experiment.

PET_C shows fast crystallization kinetics, the material almost immediately crystallizes when touching the rheometer, making it difficult to perform these measurements. As can be seen in Fig. 4c at 245 °C, the results vary completely depending on the selected specimen, and it has also been impossible to perform tests at different speeds. This indicates that we are working with a highly inhomogeneous material. However, as previously said, this does not necessarily mean that the material cannot expand.

3.1.4. Crystallinity

The thermal properties of the precursors, including T_g, T_m and crystallinity degree, have been studied according to section 2.3.4, and the results can be found in Table 2. The first heating cycle is presented in order to assess the actual thermal state of the materials before placing them into the autoclave, providing critical information for defining the appropriate foaming conditions. Additionally, thermal parameters obtained from the second heating cycle are included, as they represent the thermal behavior of the precursor materials after the same thermal history. This approach eliminates the influence of prior processing and enables a direct and consistent comparison among all samples.

The first heating cycle from DSC reveals glass transition temperatures between 70 and 80 °C, typical values for PET materials [22], presenting the PET_B the highest T_g, while T_m is around 250 °C for all the materials, being slightly higher for PET_C. The crystallinity degree is very similar for all the samples, with values lower than 12% for the extruded films. Upon analysis of the second heating cycle, only minor variations in T_g and T_m are observed. A notable exception is PET_C, which exhibits a higher T_m compared to the other materials, which may be associated with the presence of impurities or fractions with higher melting temperatures. In contrast, the degree of crystallinity shows significant differences, ranging from approximately 28 to 33%. This variation is attributed to the DSC heating program, which includes a controlled slow cooling step following the first heating cycle, promoting crystallization. The second heating cycle therefore reflects the intrinsic thermal behavior of each material, as all samples share an identical thermal history at this stage. Under these conditions, PET_C, the most degraded sample, exhibits a slightly higher degree of crystallinity. This

Table 2
Thermal characterization of the extruded materials from the first and second heating cycles from DSC.

	T_g (°C)		T_m (°C)		Crystallinity degree (%)	
	1st heating cycle	2nd heating cycle	1st heating cycle	2nd heating cycle	1st heating cycle	2nd heating cycle
PET_V	73.5 ± 0.6	79.7 ± 0.7	247.2 ± 0.6	245.5 ± 0.4	8.6 ± 1.7	28.6 ± 4.2
PET_B	78.9 ± 1.8	80.2 ± 0.3	248.3 ± 0.6	245.7 ± 0.7	6.9 ± 0.7	32.9 ± 2.9
PET_C	73.2 ± 0.3	77.4 ± 1.3	250.1 ± 0.3	249.1 ± 0.3	11.1 ± 0.4	30.2 ± 3.3

behavior can be attributed to the presence of shorter polymer chains generated during degradation, which possess enhanced mobility and, consequently, a greater ability to reorganize into crystalline domains [23].

In Fig. 5 the curves from the first and second heating of the DSC thermogram for all the solid precursors is shown.

In both heating cycles, the three thermograms exhibit comparable profiles, irrespective of whether the material is recycled or virgin. This similarity indicates that the crystalline structure is not substantially altered by the recycling process. During the first heating cycle, all samples display a cold crystallization peak at similar temperatures, a feature commonly reported for polyethylene PET materials [4]. In contrast, this peak is absent in the second heating cycle, which is consistent with the prior controlled cooling step that promotes crystallization and reduces the presence of amorphous regions capable of cold crystallization upon reheating.

3.1.5. Solubility and diffusivity

Solubility and diffusivity values are listed in Table 3. The CO_2 uptake at a saturation pressure of 15 MPa is around 6 wt % and is very similar for the three samples. Diffusivity, on the other hand, is slightly higher in the case of the pure polymer (one order of magnitude), which means that the gas is scaping faster in the virgin sample. Suggesting the impurities in recycled samples can be acting as gas barriers.

At a saturation pressure of 30 MPa, solubility is almost doubled in the case of PET_V, while in the recycled samples it increases more moderately, leading to values around 7 and 8% for PET_B and PET_C, respectively. Diffusivity increases in comparison to the values obtained at 30 MPa around one order of magnitude for all the samples in comparison to the obtained values at 15 MPa, remaining higher for the virgin polymer.

These solid-state properties are directly relevant to the subsequent foaming behavior. In particular, intrinsic viscosity influences melt strength during cell growth, crystallinity affects gas diffusion and stabilization, and gas solubility determines the nucleation potential under saturation conditions.

3.2. Cellular materials

The characteristics of the produced cellular materials will be analyzed in the following sections.

3.2.1. Crystallinity

The crystallinity degree of all the produced cellular materials as a function of the foaming temperature can be found in Fig. 6.

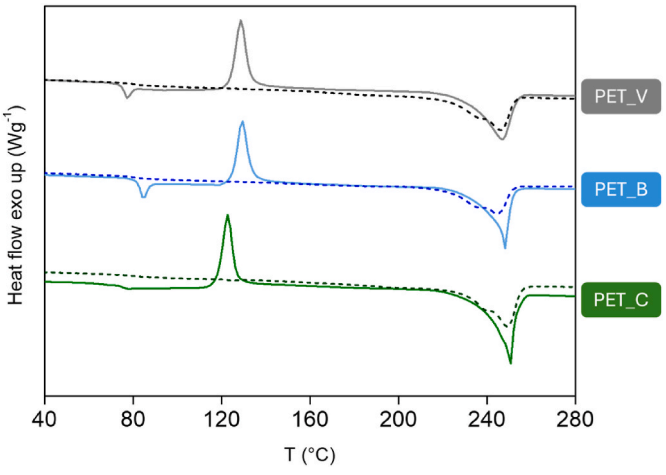

Fig. 5. First and second heating (continuous and dashed line, respectively) of the DSC from the three extruded precursors.

Table 3
Solubility and diffusivity of the materials under study saturated at 15 and 30 MPa and 50 °C.

	p_{sat} = 15 MPa		p_{sat} = 30 MPa	
	Solubility (%)	Diffusivity ($cm^2 \cdot s^{-1}$)	Solubility (%)	Diffusivity ($cm^2 \cdot s^{-1}$)
PET_V	6.04	$1.65 \cdot 10^{-12}$	11.17	$4.57 \cdot 10^{-11}$
PET_B	5.94	$3.17 \cdot 10^{-13}$	7.37	$1.32 \cdot 10^{-12}$
PET_C	6.54	$1.21 \cdot 10^{-13}$	8.06	$8.13 \cdot 10^{-12}$

The crystallinity degree of the foamed samples has increased with respect to the solid precursors, being in all cases in the range from 27 to 36%, regardless of the nature of the sample (non-recycled or recycled), foaming temperature, or saturation pressure. Furthermore, the increase in crystallinity degree and the lack of trends when varying the foaming temperature indicate that the growth in crystallinity is induced by the presence of CO_2 [24] in combination with the saturation temperature. However, as it will be discussed in the following sections, this growth in crystallinity do not hinder the foamability of these materials. On the other hand, the presence of impurities in PET_B and PET_C samples may lead to a slight increase in the crystallinity of the solid precursors (Table 2), though this is not significantly observed in the final foams. It is suggested that maximum crystallization is obtained in all cases, since these values agree with the ones from previous studies with PET [5]. Thus, the foaming conditions and the PET recycling process, even with large amounts of impurities such as in PET_C, do not worsen the crystallization of the final materials, achieving a considerable crystallinity degree.

Regarding T_g and T_m, there are no significant differences between the solid precursors and the cellular materials, and both parameters follow the same trends observed in Table 2: PET_C cellular materials present the higher melting temperatures in all the cases, regardless saturation pressure or foaming temperature, while the values of PET_V and PET_B are slightly lower, and the differences with respect to the solid precursor are within the error of the equipment, ca. 3% (Figure S1 in supporting information). Nevertheless, it is observed that there is a slight difference in the melting peak shape when increasing the foaming temperature (Fig. 7), being sharper as higher is the T_f, as well as the apparition of a small shoulder at lower temperatures, probably caused by the different quality and size of the crystals formed at those higher temperatures, suggesting that higher foaming temperatures may affect the crystal quality and population. This effect is appreciable for all materials and production conditions, the rest of the DSC thermograms can be found in Figure S1 in supporting information.

On top of that, in the DSC thermograms of the foamed samples there is not a cold crystallization peak (Fig. 7), implying that during the saturation step the PET samples are fully crystallized thanks to the CO_2 plasticization effect, achieving the highest possible crystallinity degree of ca. 30%, previously reported in other works [5], inhibiting the cold crystallization process during the DSC experiment.

3.2.2. Relative density

The relative density of all the cellular materials is shown in Fig. 8. It is observed that, independently of the material and saturation pressure, an increase in the foaming temperature leads to a reduction in the relative density, showing that at lower foaming temperatures the expansion of the materials is low, while when foaming temperatures are increased relative densities up to 0.2 are obtained regardless of the saturation pressure. Furthermore, it is observed that the general trends and values of each sample are not significantly affected by the variation in saturation pressure. Nevertheless, each sample presents particularities that must be considered. First, in PET_V, the minimum relative density is obtained at $T_f = 200$ °C, irrespective of the saturation pressure, reaching values of 0.16 and 0.18 at 15 MPa and 30 MPa, respectively. When increasing the T_f up to 220 °C, the relative density sharply

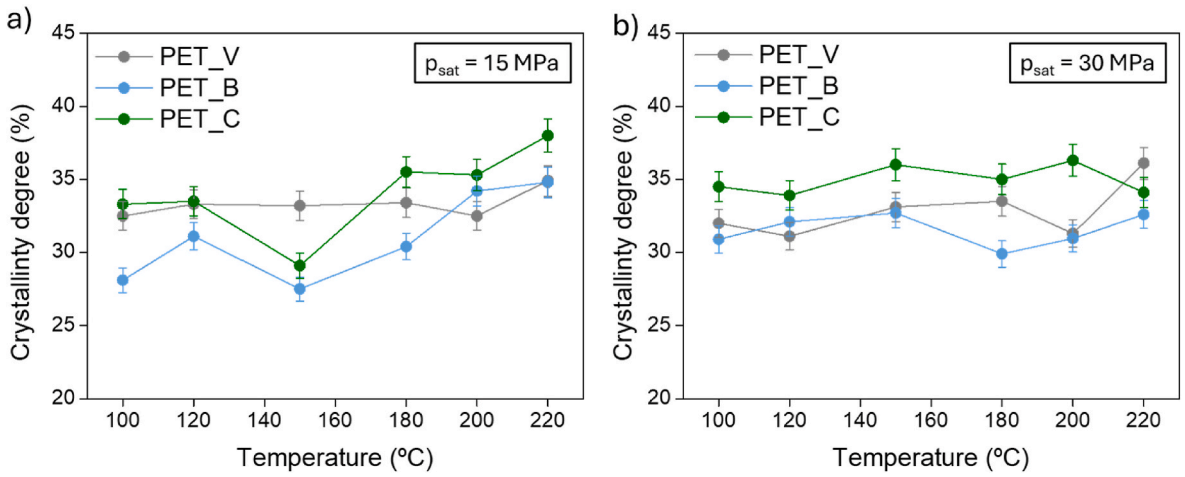

Fig. 6. Crystallinity degree of all the foamed samples saturated at a) 15 MPa and b) 30 MPa.

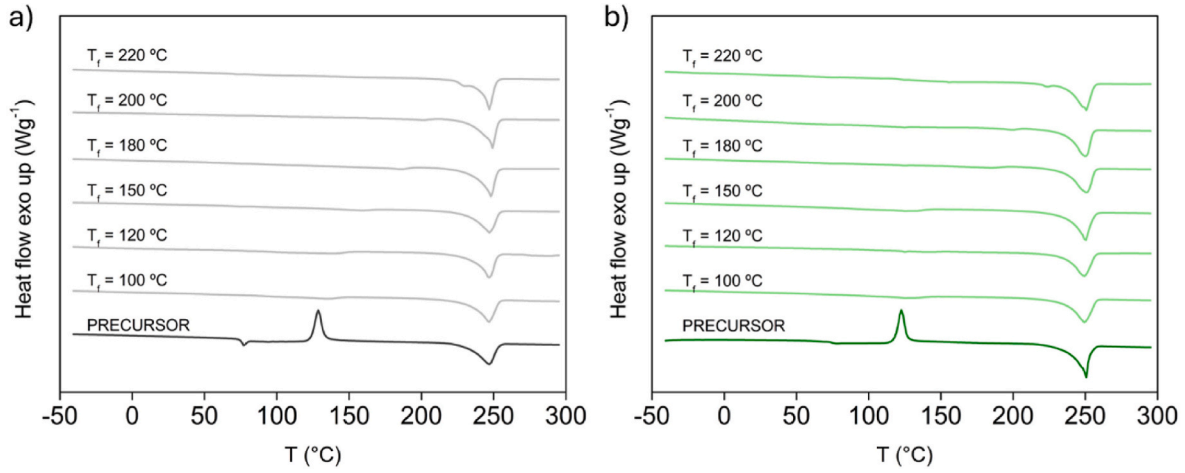

Fig. 7. First heating of the DSC thermograms of PET_V and PET_C at p_{sat} = 30 MPa, compared to the solid precursor.

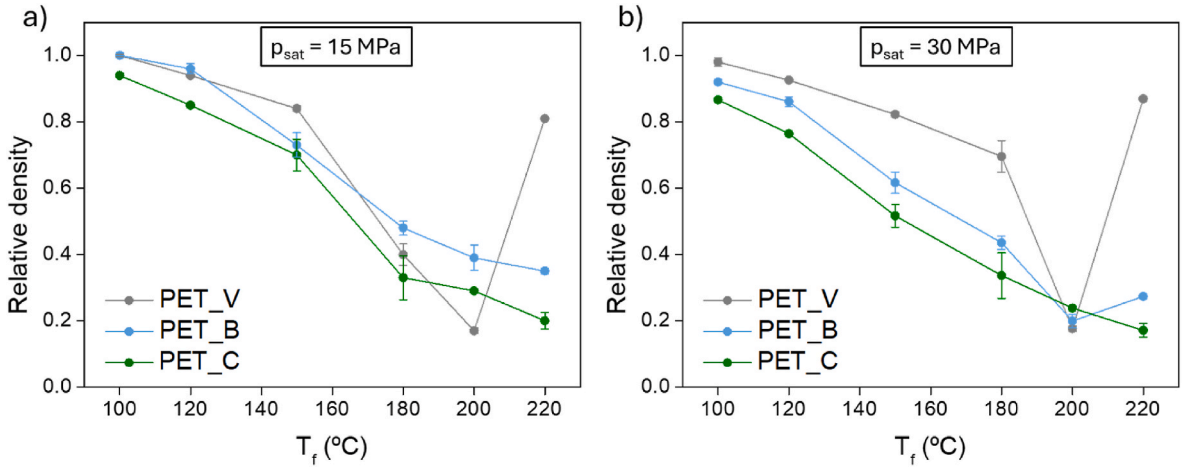

Fig. 8. Relative density of the cellular samples as a function of the foaming temperature at a saturation pressure of a) 15 MPa and b) 30 MPa.

increases, caused by collapse in the cellular structure (see section 3.2.3). On the other hand, in PET_B sample the minimum in relative density is obtained at different foaming temperatures depending on the saturation pressure: at 220 °C for p_{sat} = 15 MPa, with a value of 0.35; and at 200 °C for p_{sat} = 30 MPa, reaching a value of 0.20. Finally, in PET_C, the minimum relative density is found at T_f = 220 °C, regardless of the saturation pressure, with values of 0.20 at 15 MPa, and 0.17 at 30 MPa (the numerical data of all the samples can be found in Table S1 in the supporting information). Furthermore, it is important to highlight that both recycled materials do not show the collapse observed in virgin PET

suggesting that the recycled samples present a higher foaming stability at higher temperatures as well as indicating that a larger number of impurities seems to have a positive effect on the foaming stability, since PET_C, which is the more-contaminated sample, presents the lower relative density at $T_f = 220$ °C.

It must be noted that in all the samples the relative density starts to significantly decrease from $T_f = 180$ °C. This temperature must be reached so that mobility of the polymer chains and gas molecules starts to be significant enough to achieve reasonable expansions. In semi-crystalline polymers, the foaming temperature must be over the melting temperature of the polymer [6], thus, it is suggested that, at these conditions, the effective melting temperature caused by the presence of supercritical CO_2 [7] might be around 180 °C, and temperatures equal or higher than this one will lead to a significant expansion, therefore leading to lower relative densities.

Finally, as previously discussed both saturation pressures leads to similar results, particularly in the recycled samples. The need for lower pressure in order to obtain the same final material in terms of relative density could lead to a greener fabrication method since a lower amount of energy will be required for reaching lower pressures.

3.2.3. Cellular structure

The cellular structures obtained at $p_{sat} = 15$ MPa and T_f of 100, 150 and 200 °C for the different PETs are shown in Fig. 9. The rest of the micrographs at other foaming temperatures and saturation pressure can be found in Figure S2 and Figure S3 in the supporting information.

As can be seen, an increase in foaming temperature leads to higher expansion in all materials, however, recycled samples require from smaller temperatures to show significant cellular structure. While cellular structure appears in PET_V at 180 °C (reduction in density below this temperature is caused by macroscopic defects), PET_B and PET_C present cells even at 100 °C. This suggests that a heterogeneous nucleation process is taking place in recycled samples and lower foaming temperatures are required for cell expansion. As can be seen in Fig. 9, in the micrograph showing foamed PET_C at 100 °C, the small spheres observed in the solid (Fig. 2) can be seen inside several pores, meaning that these impurities are acting as nucleation points lowering the required temperature for expansion.

Nevertheless, this heterogeneous nucleation process does not prevent obtaining a homogeneous sample as in the case of PET_B, which, in terms of cell size distribution, is similar to the PET_V sample, which follows a homogeneous nucleation process due to the absence of impurities. On the other hand, clear bimodality is observed in PET_C, with a wider cell distribution, caused by the large amount of impurities that this sample presents. It must be considered that, even though PET_B and PET_C samples are recycled, and regardless of their rheological behavior (see section 3.1.3) both show adequate foaming behavior, leading to low density samples with a defined cellular structure.

Fig. 10 shows the different trends of cell size and nucleation density in all the samples. In the case of PET_V, only samples foamed at 180 °C or more are shown, since they are the ones having a cellular structure.

The differences between both parameters are clear depending on whether the sample is recycled or not. Regarding saturation pressure, cellular structure of PET_V, is significantly affected obtaining larger cell sizes (above 6.5 μm) and lower nucleation densities (below $10^{10}/cm^3$) at lower saturation pressures (15 MPa), while cell size decreases below 1 μm and nucleation density sharply increases up to values in the order of $10^{13}/cm^3$ when saturation pressure is increased up to 30 MPa. This strong dependence on cell size and nucleation density with saturation pressure confirms the homogeneous nucleation process that is taking place in the non-recycled sample. On the other hand, cell size and nucleation density of the recycled polymers, PET_B and PET_C, are much

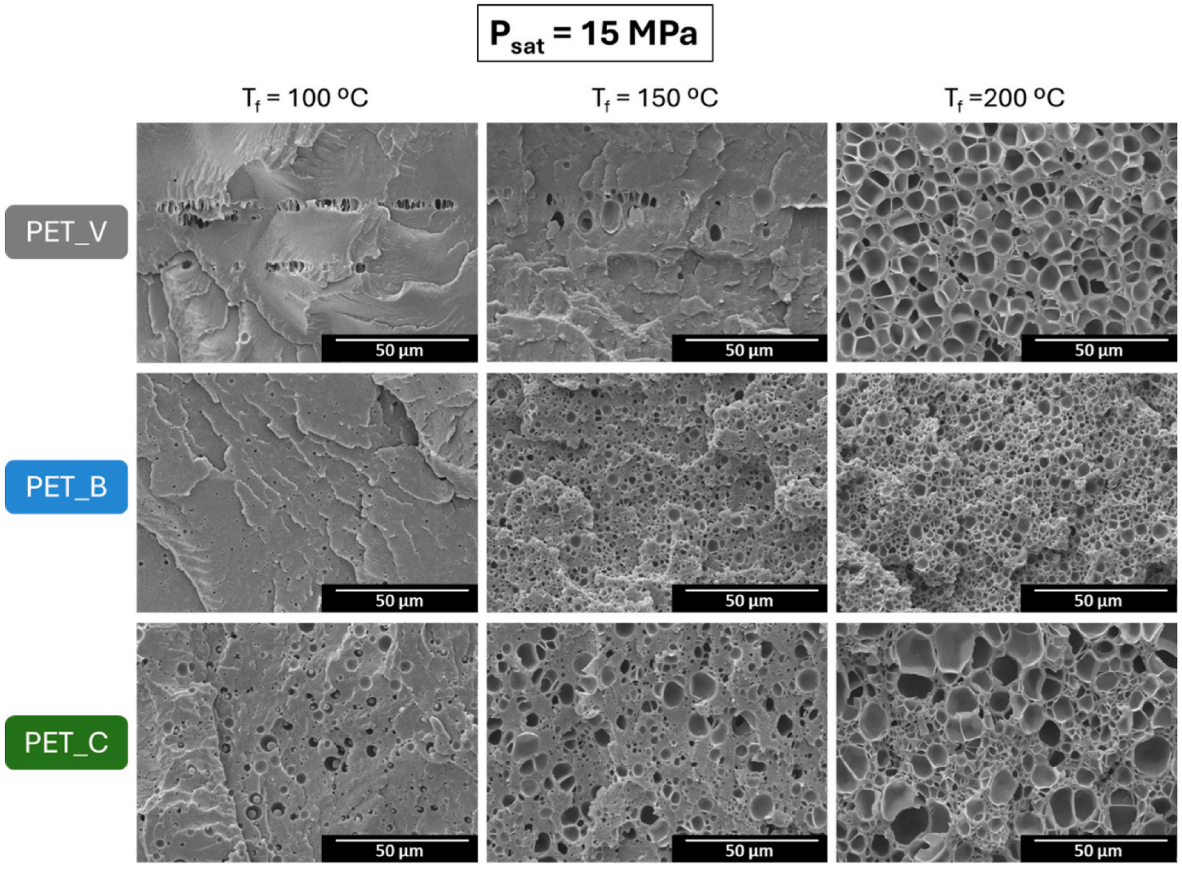

Fig. 9. SEM images from PET_V, PET_B and PET_C cellular materials foamed at 100, 150 and 200 °C, at the same saturation pressure of 15 MPa. All the images present the same magnification.

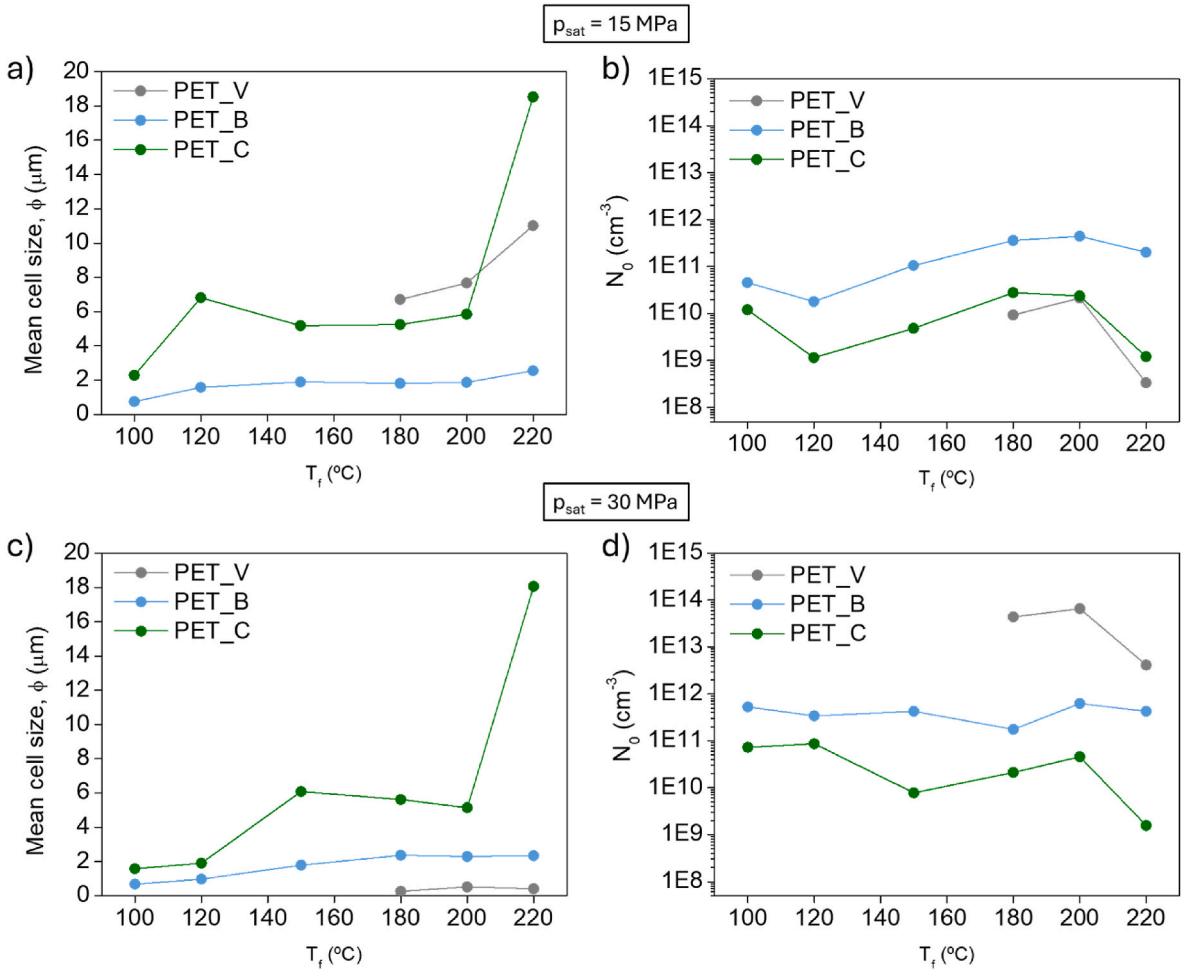

Fig. 10. A) Cell size and b) nucleation density of samples at p_{sat} = 15 MPa; c) cell size and b) nucleation density of samples at p_{sat} = 30 MPa. The error bars corresponding to the cell size measurements were omitted from the figures to improve visual clarity. These errors are provided in Table S1 of the Supporting Information.

less affected by the saturation pressure, following the same trend at both saturation pressures and reaching very similar values when foamed at the same temperatures, indicating that the nucleation process in these recycled samples is governed by the inhomogeneities, that means heterogeneous nucleation is taking place.

However, both recycled samples present differences, while at 15 MPa, relative density was similar in both samples, PET_B presents the smallest cell size, even in comparison to the pure polymer. When increasing the foaming temperature cell size remains almost constant around 2 μm, while cell nucleation density increases from $4.6{\cdot}10^{10}$ cm^{-3} at 100 °C to $4.42{\cdot}10^{11}$ cm^{-3} at 200 °C, this increase leads to the reduction of density previously discussed. PET_C presents similar trend, but with larger cell sizes around 5-6 μm and cell nucleation densities two orders of magnitude smaller. These larger cells are in agreement with the larger impurities observed in this material (Fig. 2) that control nucleation. Additionally, this material collapsed at 220 °C with a rise in the cell size and a decrease in the number of cells. Similar behavior is observed at 30 MPa.

The presence of these impurities is also transmitted to the cell size distribution (Fig. 11), while PET_V present a narrow cell size distribution, typical of a homogeneous nucleation, recycled samples present a cell size distribution given by the size distribution of the impurities. PET_C has two clear primary cell sizes in 3 and 6 μm, but it has some even bigger cells (some up to 20 μm) due to the size of some impurities. PET_B shows various cell sizes in a wide range, but smaller than that of the PET_C as previously discussed.

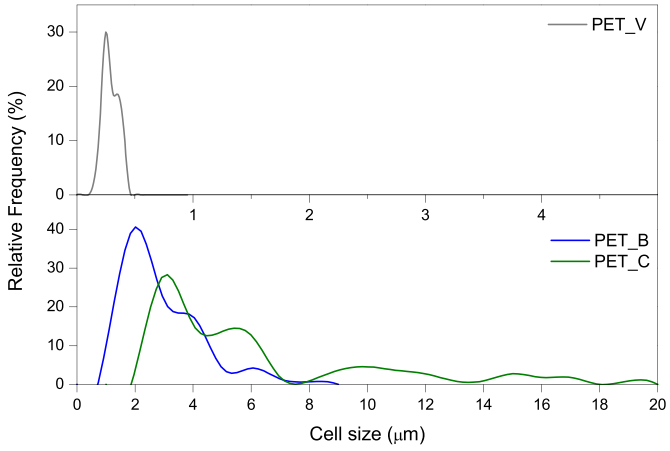

Fig. 11. Cell size distribution for samples saturated at 30 MPa and foamed at 180 °C.

To sum up, it can be concluded that the recycled PET samples allow to obtain cell sizes smaller than 10 μm combined with low relative densities up to 0.2, at low demanding saturation parameters of 15 MPa and 25 °C, even improving the values obtained with virgin PET.

3.3. 3D printed materials

The optimum foaming conditions (the ones leading to the lowest relative density) were selected to be tested on 3D printed recycled PET_B cap. This 3D printed cap presents a density of 1.26 kg/m^3, slightly lower than PET_B in film form, while its thermal properties are very similar to the PET_B in film form, with a T_g of 74.5 °C, a T_m of 250.4 °C and a crystallinity degree of 12.2%. Two experiments were performed at p_{sat} of 15 and 30 MPa and a foaming temperature of 180 °C. The comparison of the foamed cap with the initial 3D printed part is shown in Fig. 12.

It is observed that the foamed piece maintains its structural integrity and the original shape of the solid 3D printed piece, observing even each filament produced by the 3D printing process. The expansion of the piece after the foaming experiment has been analyzed by precisely measuring the piece with a caliper before and after the foaming process. This data can be found in Table 4.

As can be seen, a reduction of more than 40% in relative density in the 3D printed materials has been achieved, regardless of the saturation pressure. Although dimensional expansion occurs during foaming, such changes can be compensated at the design stage by adjusting the initial model, a common strategy in foam processing. Therefore, the observed expansion does not preclude the fabrication of dimensionally accurate components.

In Fig. 13, SEM micrographs of the 3D printed cellular materials compared with the solid 3D printed cap can be found: As observed, the solid 3D printed piece presents a solid homogeneous structure where it is possible to see the voids caused by the 3D printed filaments. On the other hand, both foamed samples present a homogeneous cellular structure, where the initial voids are still appreciable but have been reduced due to the expansion of the material in the foaming process. Furthermore, the cellular structures of both foamed samples have been evaluated according to the method described in section 2.3.6, and the results are summarized in Table 4. The cell size of the 3D foamed materials is practically identical to the ones obtained in the film-based foams (Fig. 10), observing a slight increase in the cell size when increasing the saturation pressure, as well as preserving a wide cell size distribution structure previously observed in PET_B samples (Figures S4 and S5 in supporting information). This suggests that the foaming of 3D printed materials based on rPET is possible, presenting the same foaming behavior as the same sample in film form. Furthermore, increasing the saturation pressure does not lead to a significant weight reduction or large differences in cell size. Therefore, a methodology is presented for

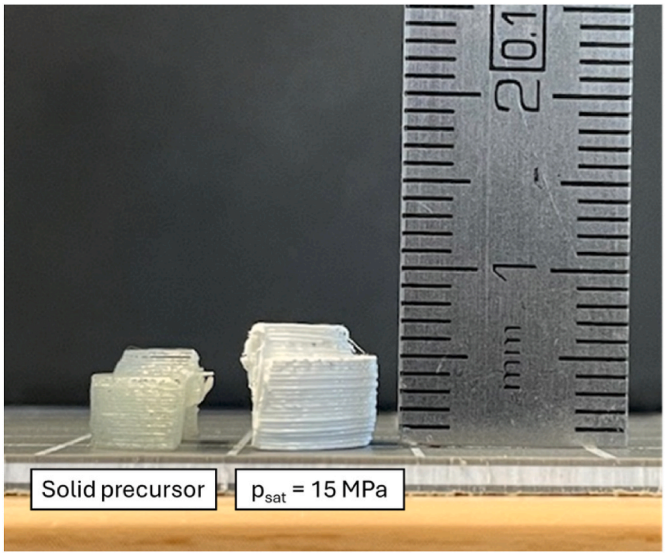

Fig. 12. Comparison between the initial 3D printed cap and the foamed part at p_{sat} of 15 MPa.

Table 4
Parameters of the foamed 3D printed material at p_{sat} = 15 and 30 MPa.

	PET_3D_15 MPa	PET_3D_30 MPa
Solid density (g/cm^3)	0.72	0.69
Relative density	0.57	0.55
Diameter expansion (%)	27.8	30.6
Height expansion (%)	24.5	37.1
Nucleation density (cm^{-3})	$1.56 \cdot 10^{11}$	$1.13 \cdot 10^{11}$
Cell size (μm)	2.1 ± 0.9	2.4 ± 1.3

reducing the weight of these materials as well as maintaining their original shape, all of which it is possible to reach at relatively mild conditions of saturation pressure and foaming temperatures. As far as the authors know, this is the first time that recycled PET-based 3D printed materials have been foamed trough gas dissolution foaming technique.

This approach adds extra value to PET upcycling through gas dissolution foaming. On the one hand, it has been demonstrated that cellular materials can be manufactured from both PET_B and PET_C, thereby expanding the range of potential applications in sector such as construction, transportation components or marine structures where PET foams are already used [25], [26]. Furthermore, it has been shown that these cellular structures, with weight reductions of up to 40% and cell sizes around 2 μm, can be transferred to 3D-printed parts without compromising their original geometry, contributing to reusing the PET in our bottles different sectors [27].

4. Conclusions

Successful foaming of two types of mixed color recycled PET, blue and color recycled PET (PET_B and PET_C), films coming from bottle residues were achieved in this work through gas dissolution foaming technique. Cellular structures even better than those obtained with virgin PET, with 2 μm of cell size and 0.28 of relative density have been obtained with PET_B through saturation at industrially scalable saturation conditions of 15 MPa and 50 °C.

After a full characterization of the precursors to compare a virgin PET with the two recycled PETs foaming, experiments were performed at two different saturation pressures, 15 and 30 MPa, and six foaming temperatures from 100 to 220 °C, making it clear that all the precursors were feasible to make cellular materials by solid state foaming. The use of a low-intrinsic-viscosity virgin PET as a rheological reference allowed isolating the role of material heterogeneity and impurities on foamability.

It was seen how, due to the impurities of the recycled materials, their CO_2 solubility was limited in comparison to the virgin polymer, and that a heterogeneous nucleation process took place instead of a homogeneous one. After the foaming process, PET_B had a more homogeneous cellular structure while PET_C had a wider distribution of cell sizes, as the impurities present in the bulk material had a broader range of sizes and were badly dispersed.

The effect of saturation pressure and foaming temperature on the cellular structure and density of the produced materials was analyzed in detail. It was found that an increase in pressure (15 to 30 MPa) did not greatly affect the resulting cellular materials in the recycled samples, while the effect of the foaming temperature was clearly seen. As temperature increased, relative density decreased up to a certain value, depending on the sample due to a rise in the cell nucleation density. The greatest density reduction in the recycled materials was achieved for PET_C foamed at 220 °C, achieving relative densities of 0.18 at 15 MPa saturation pressure and 0.17 for the ones saturated at 30 MPa. The other materials reached the best expansion ratios when foamed at 200 °C (even 180 °C for PET_B saturated at 15 MPa) achieving also minimum densities in the range of 0.2. The cellular structures found in PET_B were rather interesting, as in many cases mean cell size was around 2 μm,

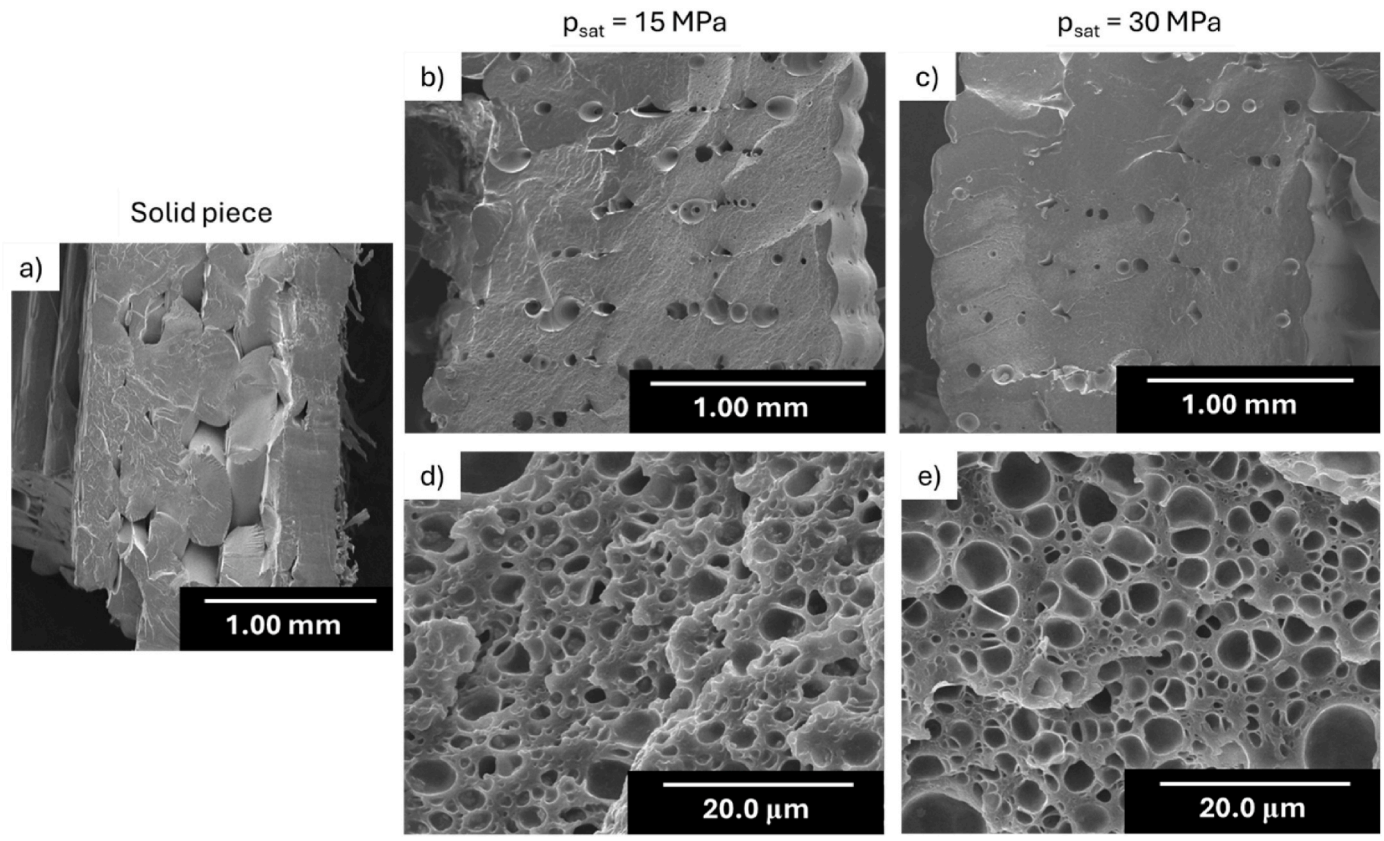

Fig. 13. SEM micrographs of the cross-section of a) solid 3D printed cap, b) cellular 3D printed cap saturated at 15 MPa, c) cellular 3D printed part saturated at 30 MPa. d) and e) are magnifications of b) and c), respectively.

while PET_C cell sizes ranged from 5 to 18 µm when foamed at the maximum temperature.

Finally, foaming experiments of a 3D printed piece based on PET_B were performed at the optimal foaming temperature and both saturation pressures. It was observed that the foamed 3D piece was expanded in all the spatial dimensions but maintaining its overall geometry. Moreover, its relative density was reduced by more than 40% and a cell size of around 2 µm was achieved regardless of the saturation pressure, suggesting that it is possible to obtain 3D printed materials based on rPET at milder conditions, leading to a more sustainable fabrication process.

These findings demonstrate that gas dissolution foaming can act as a robust, industry-compatible route for upcycling heterogeneous rPET streams into lightweight materials. The ability to foam 3D-printed rPET parts while maintaining dimensional stability highlights the potential of this approach to support circular manufacturing strategies in sectors such as transportation, construction and consumer products.

CRediT authorship contribution statement

M. Merillas: Data curation, Formal analysis, Investigation, Methodology, Visualization, Writing – original draft. **J. Lledó:** Data curation, Formal analysis, Investigation, Methodology, Visualization, Writing – original draft. **M. Santiago-Calvo:** Conceptualization, Methodology, Validation, Writing – original draft, Writing – review & editing. **L. Matesanz-Niño:** Formal analysis, Investigation, Writing – original draft, Writing – review & editing. **J. Martín-de León:** Conceptualization, Methodology, Project administration, Supervision, Validation, Visualization, Writing – original draft, Writing – review & editing. **J.C. Merino:** Conceptualization, Funding acquisition, Project administration, Resources, Supervision, Writing – review & editing. **M.A. Rodríguez-Pérez:** Conceptualization, Funding acquisition, Project administration, Resources, Supervision, Writing – review & editing.

Declaration of competing interest

The authors declare the following financial interests/personal relationships which may be considered as potential competing interests: Miguel Angel Rodriguez Perez reports financial support was provided by Spain Ministry of Science Innovation and Universities. Miguel Angel Rodriguez Perez reports financial support was provided by Government of Castile and León. Miguel Angel Rodriguez Perez reports financial support was provided by NextGeneration EU. Mercedes Santiago Calvo reports financial support was provided by Ministry of economy and competitiveness of Spain. If there are other authors, they declare that they have no known competing financial interests or personal relationships that could have appeared to influence the work reported in this paper.

Acknowledgments

Grant PID2024-157392OB-I00 funded by MICIU/AEI/10.13039/501100011033 and by ERDF/EU. Grant PDC2025-165502-I00 funded by MICIU/AEI/10.13039/501100011033 and by the European Union through NextGenerationEU/PRTR. Financial support from the Junta de Castilla y León and FEDER funds is gratefully acknowledged (Reference: CLU-2025-2-05). Financial support from the Ministry of Economy and Competitiveness (MINECO), Spain, through the PTQ2021-011628 project (M. Santiago-Calvo) is gratefully acknowledged.

Appendix A. Supplementary data

Supplementary data to this article can be found online at https://doi.org/10.1016/j.mtsust.2026.101352.

Data availability

Data will be made available on request.

References

[1] Statista [Online]. Available: https://www.statista.com/statistics/1479044/share-of-global-demand-for-plastics-by-type/.

[2] J. Vaucher, A. Demongeot, V. Michaud, Y. Leterrier, Recycling of bottle grade PET: influence of HDPE contamination on the microstructure and mechanical performance of 3D printed parts, Polymers 14 (24) (Dec. 2022), https://doi.org/10.3390/polym14245507.

[3] P.P.K. Amandeep Singh, S.L. Banerjee, K. Kumari, Recent innovations in chemical recycling of polyethylene terephthalate waste: a circular economy approach toward sustainability, in: Handbook of Solid Waste Management: Sustainability Through Circular Economy, July 2024, 2022, pp. 1–2336, https://doi.org/10.1007/978-981-16-4230-2.

[4] P.M. Nguyen, C. Berrard, N. Daoud, P. Saillard, J. Peyroux, O. Vitrac, Assessment of chemical risks and circular economy implications of recycled PET in food packaging with functional barriers, Resources, Environment and Sustainability 17 (February) (2024) 100163, https://doi.org/10.1016/j.resenv.2024.100163.

[5] A.C. Enache, I. Grecu, P. Samoila, Polyethylene terephthalate (PET) recycled by catalytic glycolysis: a Bridge toward circular economy principles, Materials 17 (12) (2024), https://doi.org/10.3390/ma17122991.

[6] L.M. Sherman, Compatibilizers Aid Recycling & Upcycling of Mixed Resins: compatibilizers are proving their worth in boosting critical properties such as impact/stiffness balance of PCR and PIR blends of polyolefins and other plastics, Plast. Technol. 68 (7) (2022).

[7] D.G. Kulas, A. Zolghadr, U.S. Chaudhari, D.R. Shonnard, Economic and environmental analysis of plastics pyrolysis after secondary sortation of mixed plastic waste, J. Clean. Prod. 384 (November 2022) (2023) 135542, https://doi.org/10.1016/j.jclepro.2022.135542.

[8] M. Azevedo, A. Moore, M. Van Hoey, Capturing the green-premium value from sustainable materials | McKinsey, McKinsey (October) (2022) [Online]. Available: https://www.mckinsey.com/industries/metals-and-mining/our-insights/capturing-the-green-premium-value-from-sustainable-materials.

[9] K. Bocz, et al., Recycled PET foaming: supercritical carbon dioxide assisted extrusion with real-time quality monitoring, Adv. Ind. Eng. Polym. Res. 4 (3) (2021) 178–186, https://doi.org/10.1016/j.aiepr.2021.03.002.

[10] S. Yao, T. Guo, T. Liu, Z. Xi, Z. Xu, L. Zhao, Good extrusion foaming performance of long-chain branched PET induced by its enhanced crystallization property, J. Appl. Polym. Sci. 137 (41) (2020) 1–16, https://doi.org/10.1002/app.49268.

[11] K. Bocz, B. Molnár, G. Marosi, F. Ronkay, Preparation of low-density microcellular foams from recycled PET modified by solid State polymerization and chain extension, J. Polym. Environ. 27 (2) (2019) 343–351, https://doi.org/10.1007/s10924-018-1351-z.

[12] Y. Chen, S. Yao, Y. Ling, W. Zhong, D. Hu, L. Zhao, Microcellular PETs with high expansion ratio produced by supercritical CO2 molding compression foaming process and their mechanical properties, Adv. Eng. Mater. 24 (3) (Mar. 2022), https://doi.org/10.1002/adem.202101124.

[13] N. Lukács, F. Ronkay, B. Molnár, B. Marosfői, K. Bocz, Characterisation of flame retarded recycled PET foams produced by batch foaming, Polym. Test. 124 (Jul) (2023), https://doi.org/10.1016/j.polymertesting.2023.108104.

[14] B. Wunderlich, Thermal Analysis, Elsevier, 1990, https://doi.org/10.1016/C2012-0-01687-0.

[15] B. Wunderlich, Differential THERMAL ANALYSIS, Thermal Analysis (1990) 123–218, https://doi.org/10.1016/B978-0-12-765605-2.50008-X.

[16] H. Guo, V. Kumar, Some thermodynamic and kinetic low-temperature properties of the PC-CO2 system and morphological characteristics of solid-state PC nanofoams produced with liquid CO2, Polymer (Guildf). 56 (Jan. 2015) 46–56, https://doi.org/10.1016/j.polymer.2014.09.061.

[17] J. Crank, The Mathematics of Diffusion, second ed., Brunel University Uxbridge: Claredon Press, Oxford, 1975.

[18] J. Torre, S. Barroso-Solares, M.A. Rodríguez-Pérez, J. Pinto, On the use of neural networks for the structural characterization of polymeric porous materials, Polymer (Guildf). 291 (November 2023) (2024), https://doi.org/10.1016/j.polymer.2023.126597.

[19] C. Carrot, S. Mbarek, M. Jaziri, Y. Chalamet, C. Raveyre, F. Prochazka, Immiscible blends of PC and PET, current knowledge and new results: rheological properties, Macromol. Mater. Eng. 292 (6) (2007) 693–706, https://doi.org/10.1002/mame.200700006.

[20] C. Carrot, S. Mbarek, M. Jaziri, Y. Chalamet, C. Raveyre, F. Prochazka, Immiscible blends of PC and PET, current knowledge and new results: rheological properties, Macromol. Mater. Eng. 292 (6) (Jun. 2007) 693–706, https://doi.org/10.1002/mame.200700006.

[21] E. Laguna-Gutierrez, A. Lopez-Gil, C. Saiz-Arroyo, R. Van Hooghten, P. Moldenaers, M.A. Rodriguez-Perez, Extensional rheology, cellular structure, mechanical behavior relationships in HMS PP/montmorillonite foams with similar densities, J. Polym. Res. 23 (12) (Dec. 2016), https://doi.org/10.1007/s10965-016-1143-x.

[22] B. Lepoittevin and P. Roger, "Poly(Ethylene Terephthalate)," pp. 97–126. .

[23] R. W. Nunes, J. R. Martin, and J. F. Johnson, "Influence of Molecular Weight and Molecular Weight Distribution on Mechanical Properties of Polymers." .

[24] D.F. Baldwin, M. Shimbo, N.P. Suh, The role of gas dissolution and induced crystallization during microcellular polymer processing: a study of poly(ethylene terephthalate) and carbon dioxide systems, Journal of Engineering Materials and Technology, Transactions of the ASME 117 (1) (1995) 62–74, https://doi.org/10.1115/1.2804373.

[25] S. Mandegarian, M. Hojjati, Recycled PET foam core sandwich panels with reinforced hybrid composite facesheets : a sustainable approach for enhanced impact resistance 27 (2) (2025) 396–428, https://doi.org/10.1177/10996362241298164.

[26] P. Mazzuca, Flexural behaviour of GFRP sandwich panels with eco-friendly PET foam core for the rehabilitation of building floors, Structures 60 (July 2023) (2024) 105815, https://doi.org/10.1016/j.istruc.2023.105815.

[27] L. Toth, E. Slezák, K. Bocz, F. Ronkay, Progress in 3D printing of recycled PET, Mater. Today Sustain. 26 (January) (2024), https://doi.org/10.1016/j.mtsust.2024.100757.